Nanoscale Advances

ROYAL SOCIETY OF CHEMISTRY

PAPER

View Article Online
View Journal | View Issue

Cite this: *Nanoscale Adv.*, 2024, **6**, 3624

First-principles investigations of the controllable electronic properties and contact types of type II $MoTe_2/MoS_2$ van der Waals heterostructures

Son T. Nguyen,[a] Nguyen V. Hieu,[b] Huy Le-Quoc,[c] Kien Nguyen-Ba,*[c] Chuong V. Nguyen,[d] Huynh V. Phuc[e] and Cuong Q. Nguyen*[fg]

Two-dimensional (2D) van der Waals (vdW) heterostructures are considered as promising candidates for realizing multifunctional applications, including photodetectors, field effect transistors and solar cells. In this work, we performed first-principles calculations to design a 2D vdW $MoTe_2/MoS_2$ heterostructure and investigate its electronic properties, contact types and the impact of an electric field and in-plane biaxial strain. We find that the $MoTe_2/MoS_2$ heterostructure is predicted to be structurally, thermally and mechanically stable. It is obvious that the weak vdW interactions are mainly dominated at the interface of the $MoTe_2/MoS_2$ heterostructure and thus it can be synthesized in recent experiments by the transfer method or chemical vapor deposition. The construction of the vdW $MoTe_2/MoS_2$ heterostructure forms a staggered type II band alignment, effectively separating the electrons and holes at the interface and thereby extending the carrier lifetime. Interestingly, the electronic properties and contact types of the type II vdW $MoTe_2/MoS_2$ heterostructure can be tailored under the application of external conditions, including an electric field and in-plane biaxial strain. The semiconductor–semimetal–metal transition and type II–type I conversion can be achieved in the vdW $MoTe_2/MoS_2$ heterostructure. Our findings underscore the potential of the vdW $MoTe_2/MoS_2$ heterostructure for the design and fabrication of multifunctional applications, including electronics and optoelectronics.

Received 5th March 2024
Accepted 20th May 2024

DOI: 10.1039/d4na00193a

rsc.li/nanoscale-advances

1 Introduction

The advent of two-dimensional (2D) materials, characterized by their atomic structures and unique properties, has ushered in a new era of exploration and innovation in condensed matter physics and materials science. This burgeoning class of materials, with graphene[1] as a pioneering example, has captivated both fundamental and industrial researchers. Following the success of graphene, a plethora of 2D materials have been exfoliated and investigated, both in terms of fundamental understanding and practical applications. Recently, the most extensively investigated 2D materials are transition metal mono- and di-chalcogenides,[2–5] MXenes[6–8] and graphitic carbon nitrides.[9–11] The versatility in the electronic and optical properties of 2D materials makes them promising candidates for multiple applications, ranging from advanced electronics to quantum computing and beyond.[12–15]

More interestingly, the special versatility of 2D materials lies in their potential for creating 2D vdW heterostructures by stacking them together.[16–18] The 2D vdW heterostructures based on 2D materials offer an intriguing platform for tailoring and enhancing material properties, unlocking novel phenomena, and paving the way for practical applications in next-generation devices.[19–21] Recently, a plethora of 2D vdW heterostructures have been synthesized experimentally and explored computationally, for instance, TMD heterostructures,[22,23] MXene heterostructures,[24,25] MA_2Z_4 heterostructures[26,27] and phosphorene heterostructures.[28–30] Among them, the exploration of vdW heterostructures between different 2D TMD materials has received much more consideration and interest. Many 2D TMD-based vdW heterostructures have been successfully fabricated and explored, such as MoS_2/WSe_2,[31,32] HfS_2/MoS_2,[33] MoS_2/WS_2,[34] $MoTe_2/ReS_2$ (ref. 35) and black phosphorus/MoS_2.[36] One can find that the 2D vdW TMD heterostructures can be synthesized in experiments by various strategies, including top-down[37] and bottom-up[38,39] strategies.

Recently, a novel 2D vdW heterostructure based on $MoTe_2$ and MoS_2 TMD materials has been successfully fabricated in

[a]Faculty of Electrical Engineering, Hanoi University of Industry, Hanoi 100000, Vietnam. E-mail: nguyensontung@haui.edu.vn
[b]The University of Danang – University of Science and Education, Da Nang 550000, Vietnam
[c]The University of Danang – University of Science and Technology, Danang 550000, Vietnam. E-mail: nbkien@dut.udn.vn
[d]Department of Materials Science and Engineering, Le Quy Don Technical University, Hanoi 100000, Vietnam
[e]Division of Theoretical Physics, Dong Thap University, Cao Lanh 870000, Vietnam
[f]Institute of Research and Development, Duy Tan University, Da Nang 550000, Vietnam. E-mail: nguyenquangcuong3@duytan.edu.vn
[g]Faculty of Natural Sciences, Duy Tan University, Da Nang 550000, Vietnam

experiments by various methods, such as one-step CVD,[40] mechanical exfoliation[41,42] and direct imprinting.[43] Using the one-step CVD technique, Ding *et al.*[40] fabricated a $MoTe_2/MoS_2$ heterostructure and demonstrated that the photodetector based on such a heterostructure exhibits outstanding photoresponsivity and external quantum efficiency. Lately, Ji *et al.*,[41] utilizing mechanical exfoliation, fabricated a 2D vdW $MoTe_2/MoS_2$ heterostructure. These findings proved that such a heterostructure can be considered as a promising candidate for optoelectronic devices and integrated photonics. In addition, the $MoTe_2/MoS_2$ heterostructure can also be fabricated by combining the mechanical exfoliation and transfer methods[42] or direct imprinting.[43] All these experimental findings highlighted the potential applications of $MoTe_2/MoS_2$ heterostructures for multifunctional devices, including electronics and optoelectronics. Despite experimental successes in the fabrication of $MoTe_2/MoS_2$ heterostructures, a comprehensive computational investigation into the depth of their atomic structure, electronic properties and the formation of contact types is notably lacking. Therefore, in this work, we perform first-principles calculations to design a $MoTe_2/MoS_2$ heterostructure and investigate its structures and electronic properties and the formation of type II band alignment. The impact of external conditions is also explored to examine the potential applications of the $MoTe_2/MoS_2$ heterostructure for multifunctional devices. Our findings underscore the potential of the vdW $MoTe_2/MoS_2$ heterostructure for the design and fabrication of multifunctional applications, including electronics and optoelectronics.

2 Computational methods

In this work, the first-principles calculations are performed using the Quantum Espresso simulation package.[44,45] The geometric optimization process and electronic property calculations are performed in the framework of the Perdew–Burke–Ernzerhof (PBE) functional[46] within the projector augmented-wave (PAW) pseudopotential.[47] A cut-off energy of 510 eV and a Monkhorst–Pack ($9 \times 9 \times 1$) *K*-point mesh are employed for all the processes and calculations. The hybrid Heyd–Scuseria–Ernzerhof (HSE) functional[48] is also employed to get a more accurate band gap value of materials. The weak vdW interactions that may occur in layered materials can be described by adding the long-range dispersion correction of the Grimme DFT-D3 method.[49] The convergence threshold for the force and energy in all the calculations is set at 0.01 eV $Å^{-1}$ and 10^{-6} eV, respectively. A vacuum thickness of 27 Å is applied along the *z* direction of materials to avoid any unnecessary interlayer interactions. A dipole correction is also employed for all the calculation processes.

3 Results and discussion

We first investigate the atomic structure and electronic properties of MoX_2 (X = Te, S) monolayers. The atomic structures of MoX_2 are depicted in Fig. 1. The MoX_2 monolayer consists of an X–Mo–X layer, where a Mo atom is sandwiched between two X atoms on different sides. Similar to graphene, the MoX_2 monolayer shows a hexagonal atomic structure. The lattice parameters of $MoTe_2$ and MoS_2 monolayers are calculated to be 3.50 and 3.16 Å, respectively. These values are consistent with the experimental measurement.[50] The electronic band structures of MoS_2 and $MoTe_2$ monolayers are depicted in Fig. 1(c) and (d). Both MoS_2 and $MoTe_2$ monolayers exhibit semiconducting behavior with a direct band gap. The valence band maximum (VBM) and conduction band minimum (CBM) are located at the *K* point for both the MoS_2 and $MoTe_2$ monolayers. The calculated band gaps of the MoS_2 and $MoTe_2$ monolayers are 1.78/2.26 and 1.19/1.65 eV given by the PBE/HSE functional, respectively. It is obvious that the traditional PBE functional underestimates the band gap of 2D materials, while the hybrid HSE06 can provide a more accurate band gap. However, both

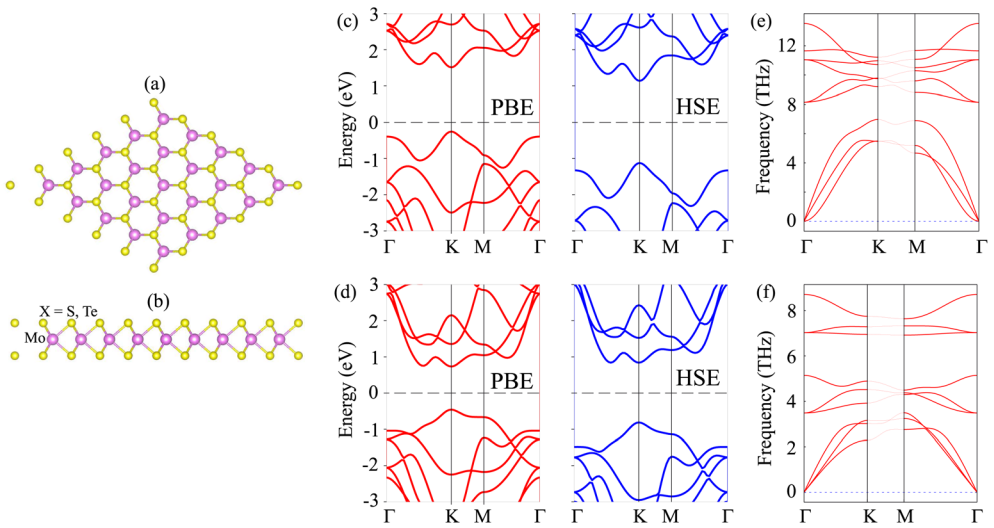

Fig. 1 (a) Top view and (b) side view of the atomic structures of a MoX_2 (X = S, Te) monolayer. Calculated electronic band structures of (c) MoS_2 and (d) $MoTe_2$ monolayers from PBE and HSE functionals. Phonon spectrum of (e) MoS_2 and (f) $MoTe_2$ monolayers.

the PBE and HSE06 functionals yield consistent behavior for the MoS_2 and $MoTe_2$ monolayers. Hence, we employed the PBE functional for the subsequent calculations due to its low computational resource. The phononic spectrum of MoS_2 and $MoTe_2$ monolayers is illustrated in Fig. 1(e) and (f). One can observe that there are no negative frequencies in the phonon spectrum of both the MoS_2 and $MoTe_2$ monolayers, predicting that these monolayers are dynamically stable.

The atomic structures of the $MoTe_2/MoS_2$ heterostructure are illustrated in Fig. 2. The $MoTe_2/MoS_2$ heterostructure is designed by using (2×2) unit cells of a MoS_2 monolayer and $(\sqrt{3} \times \sqrt{3})$ unit cells of a $MoTe_2$ monolayer. The lattice mismatch is calculated to be 2.1%, which is small and can be considered negligible. After geometric optimization, the interlayer spacing d between the two constituent $MoTe_2$ and MoS_2 monolayers is obtained to be 3.33 Å. This interlayer spacing is consistent with that in other typical vdW heterostructures[51–53] and the experimental value.[42] This indicates that the $MoTe_2/MoS_2$ heterostructure is characterized by weak vdW interactions. Furthermore, to examine the stability of the $MoTe_2/MoS_2$ heterostructure, we calculate the binding energy as follows:

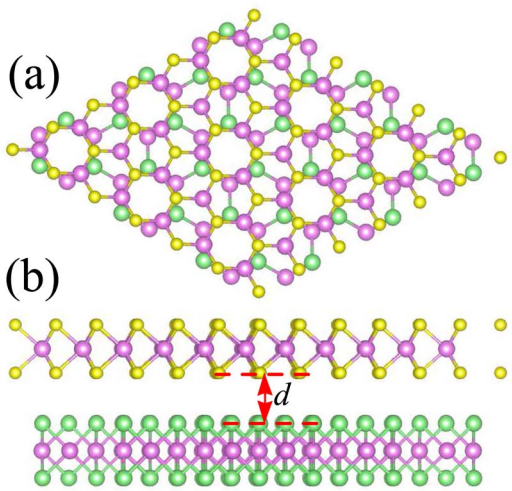

Fig. 2 (a) Top view and (b) side view of the atomic structure of the $MoTe_2/MoS_2$ heterostructure.

$$E_b = \frac{E_H - \sum E_M}{A} \quad (1)$$

Here, E_H and E_M are the total energies of the $MoTe_2/MoS_2$ heterostructure and isolated MoX_2 (X = S, Te) monolayers, respectively. A stands for the surface area of the heterostructure. The E_b of the $MoTe_2/MoS_2$ heterostructure is obtained to be -32.23 meV Å^{-2}. The negative value of the binding energy indicates that the $MoTe_2/MoS_2$ heterostructure is structurally stable. In addition, we find that the value of the binding energy is consistent with that in graphite[54] and other vdW-based systems.[55,56] All these findings confirm that the weak vdW interactions are mainly dominated at the interface of the $MoTe_2/MoS_2$ heterostructure. It is noteworthy that the weak vdW interactions keep the $MoTe_2/MoS_2$ heterostructure stable and can be synthesized in recent experiments by the transfer method[42] or chemical vapor deposition (CVD) method.[40]

Furthermore, to check the thermal and mechanical stability of the $MoTe_2/MoS_2$ heterostructure, we perform *Ab initio* molecular dynamics (AIMD) simulation and elastic constant calculation. The fluctuation in the total energy as a function of time steps of the $MoTe_2/MoS_2$ heterostructure is depicted in Fig. 3(a). It is evident that the change in the total energy of the $MoTe_2/MoS_2$ heterostructure before and after heating for 6 ps is small. Additionally, there is no distortion in the atomic structure of the $MoTe_2/MoS_2$ heterostructure after heating for 6 ps. All these findings confirm that the $MoTe_2/MoS_2$ heterostructure is thermally stable at room temperature of 300 K. The elastic constants C_{ij} of the $MoTe_2/MoS_2$ heterostructure are also calculated to evaluate its mechanical stability. The elastic constants of the $MoTe_2/MoS_2$ heterostructure are depicted in Fig. 3(b). The elastic constants of the constituent $MoTe_2$ and MoS_2 monolayers are also calculated for comparison. The calculated C_{11}, C_{12} and C_{66} of the $MoTe_2/MoS_2$ heterostructure are 264.18, 49.17 and 107.50 N m^{-1}, respectively. One can find that these values of the elastic constants satisfy the Born-Huang criteria,[57] confirming that the heterostructure is mechanically stable. Furthermore, it is evident that the elastic constants of the $MoTe_2/MoS_2$ heterostructure exhibit a substantial enhancement compared to those in the constituent monolayers. Besides, the Young's modulus of the $MoTe_2/MoS_2$ heterostructure is also greater than that of the $MoTe_2$ and MoS_2

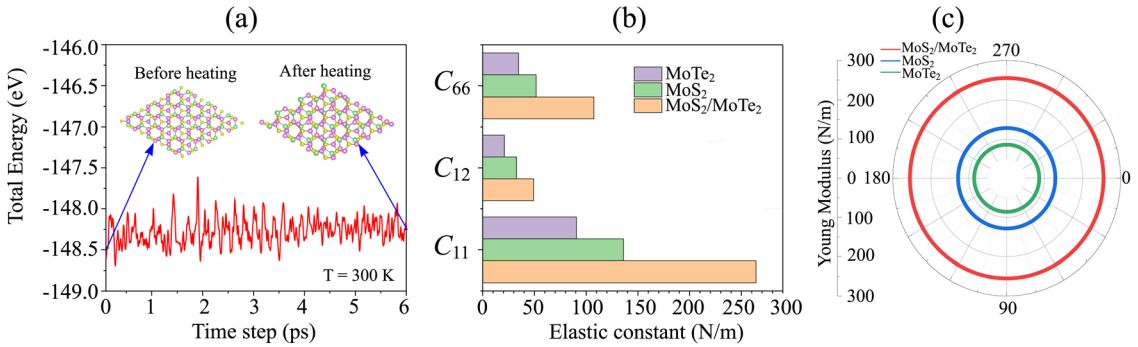

Fig. 3 (a) The fluctuation in the total energy as a function of time steps of the $MoTe_2/MoS_2$ heterostructure. The insets show the atomic structures of the $MoTe_2/MoS_2$ heterostructure before and after heating for 6 ps. (b) Elastic constants and (c) angle-dependent Young's modulus of the $MoTe_2/MoS_2$ heterostructure and the isolated $MoTe_2$ and MoS_2 constituent monolayers.

monolayers, exhibiting that the construction of the $MoTe_2$/MoS_2 heterostructure leads to an enhancement in the in-plane stiffness, as depicted in Fig. 3(c).

The projected band structure of the $MoTe_2$/MoS_2 heterostructure is depicted in Fig. 4(a). The $MoTe_2$/MoS_2 heterostructure possesses a semiconducting behavior with an indirect band gap. The VBM is located at the Γ point, whereas the CBM is at the K point. The band gap of the $MoTe_2$/MoS_2 heterostructure is 0.97 eV. Such a band gap is still smaller than that of both the constituent $MoTe_2$ and MoS_2 monolayers. This implies that the formation of the $MoTe_2$/MoS_2 heterostructure gives rise to a reduction in the band gap. A narrower band gap corresponds to stronger optical absorption. Therefore, the construction of the $MoTe_2$/MoS_2 heterostructure could lead to an enhancement in the optical properties. More interestingly, the band edges of the $MoTe_2$/MoS_2 heterostructure are contributed by distinct layers. The VBM is mainly contributed by the $MoTe_2$ layer, while the CBM comes from the MoS_2 layer. This finding suggests that the $MoTe_2$/MoS_2 heterostructure forms a type II band alignment. The formation of a type II band alignment was also observed in previous experiments.[41,42] Therefore, the type II $MoTe_2$/MoS_2 heterostructure can be considered as a promising candidate for the design of optoelectronic and electronic devices, such as photodetectors and transistors.

We further consider the charge redistribution at the interface of the $MoTe_2$/MoS_2 heterostructure by analyzing the charge density difference (CDD) as follows:

$$\Delta\rho = \rho_H - \sum \rho_M \quad (2)$$

Here, ρ_H and ρ_M are the charge densities of the $MoTe_2$/MoS_2 heterostructure and isolated MoX_2 (X = S, Se) monolayers, respectively. The planar-averaged CDD of the $MoTe_2$/MoS_2 heterostructure is depicted in Fig. 4(b). The dark blue and dark orange regions represent charge accumulation and depletion, respectively. It is evident that the charges are mainly accumulated in the $MoTe_2$ layer and depleted in the MoS_2 layer. It indicates that the $MoTe_2$ gains electrons, while the MoS_2 layer loses electrons. The electrons flow from the MoS_2 to the $MoTe_2$ layer, whereas the holes are transferred in the opposite direction, *i.e.* from the $MoTe_2$ to the MoS_2 layer. Bader charge analysis indicates that there is a small amount of charge transfer of about 10^{-3} electrons between the two constituent layers. Furthermore, to confirm the charge transfers in the $MoTe_2$/MoS_2 heterostructure, we also calculate the work functions of the $MoTe_2$/MoS_2 heterostructure and the constituent MoX_2 monolayers. The work function of a material can be calculated as: $\Phi = E_{vac} - E_F$, where E_{vac} and E_F represent the vacuum energy and Fermi energy, respectively. The work functions of the $MoTe_2$ and MoS_2 monolayers are calculated to be 4.76 eV and 4.08 eV, respectively. The lower work function of the MoS_2 monolayer compared to that of the $MoTe_2$ monolayer confirms that the electrons move from the MoS_2 to the $MoTe_2$ layer upon the formation of the heterostructure. The work function of the $MoTe_2$/MoS_2 heterostructure is calculated to be 4.98 eV, which is larger than that of the MoS_2 and $MoTe_2$ layers. The electrostatic potential of the $MoTe_2$/MoS_2 heterostructure is displayed in Fig. 4(c). One can find that the difference in the potential of the MoS_2 and $MoTe_2$ layers is small, verifying a small amount of charge transfer between the two layers. In addition, the potential of the MoS_2 layer is deeper than that of the $MoTe_2$ layer, confirming that the electrons move from the MoS_2 to the $MoTe_2$ layer. Such charge transfer leads to the formation of a built-in electric field, pointing from the MoS_2 to the $MoTe_2$ layer in their combined heterostructure.

Furthermore, we examine how the external conditions impact the electronic properties and contact types of the $MoTe_2$/MoS_2 heterostructure. Therefore, external electric fields and biaxial strains are applied to the heterostructure. The electric fields are applied along the z direction of the heterostructure, as depicted in the inset of Fig. 5(a). The positive direction of the electric fields is defined as from the $MoTe_2$ to the MoS_2 layer in their combined heterostructure. It is evident that an electric field can be used to modify the band gaps and change the contact types in the $MoTe_2$/MoS_2 heterostructure, as shown in Fig. 5(a). The band gap of the $MoTe_2$/MoS_2 heterostructure increases with applying a negative electric field and decreases with applying a positive electric field. The physical mechanism of such change can be described as follows: the direction of the built-in electric field is opposite to that of the negative electric

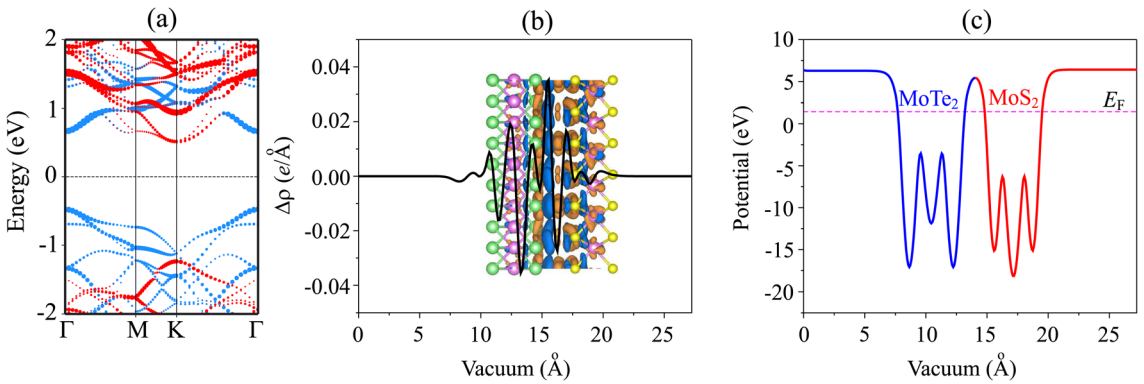

Fig. 4 (a) Projected band structure, (b) planar-averaged charge density difference and (c) electrostatic potential of the $MoTe_2$/MoS_2 heterostructure. Red and blue balls stand for the contributions of the MoS_2 and $MoTe_2$ layers, respectively. The dark blue and dark orange represent the charge accumulation and depletion, respectively.

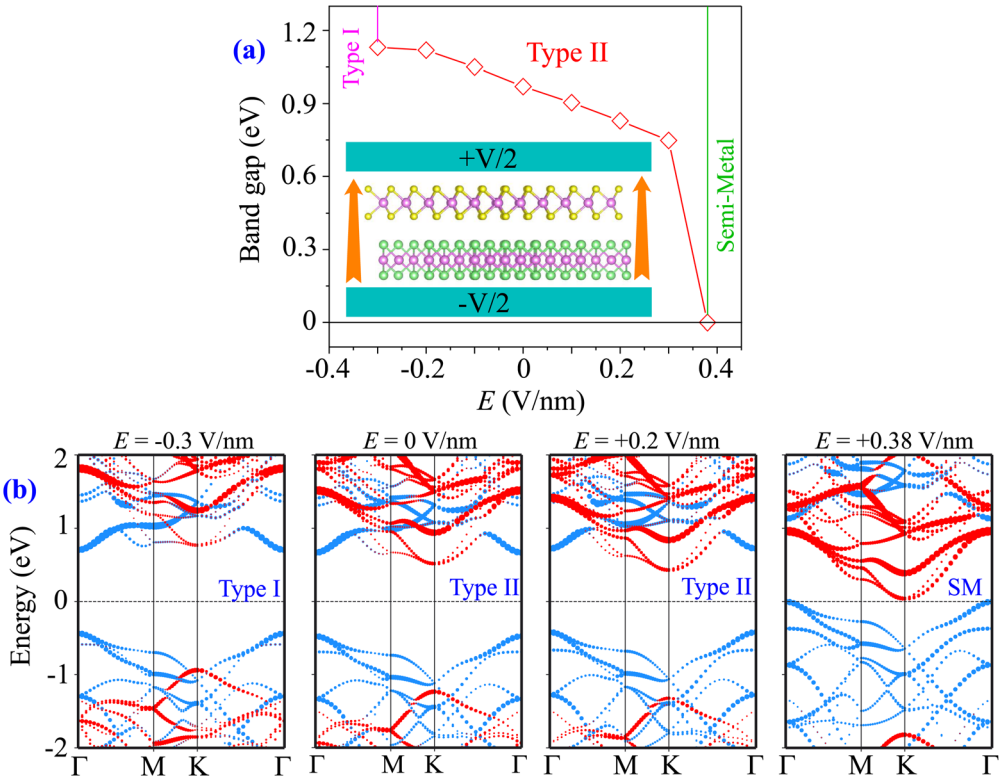

Fig. 5 (a) The variation of the band gaps and (b) the projected band structures of the $MoTe_2/MoS_2$ heterostructure under electric fields of different strengths. The inset shows the schematic model of applied electric fields along the *z* direction of the heterostructure.

field. Thus, the negative electric field can give rise to an enhancement in the band gap of the $MoTe_2/MoS_2$ heterostructure because the total electric field is weakened. On the other hand, the direction of the built-in electric field and positive electric field is the same. The total electric field is strengthened. Thus, the positive electric field causes a reduction in the band gap of the $MoTe_2/MoS_2$ heterostructure. The negative electric field can also lead to the transition from type II to type I band alignment, while the positive electric field gives rise to the semiconductor to semimetal transition. The underlying mechanism of these transitions can be described by analyzing the projected band structures of the $MoTe_2/MoS_2$ heterostructure under electric fields of different strengths, as depicted in Fig. 5(b). At a critical strength of the negative electric field of -0.3 V nm^{-1}, the CBM of the $MoTe_2/MoS_2$ heterostructure is located at the Γ point, as shown in Fig. 5(b). Such a CBM is contributed by the $MoTe_2$ layer, indicating that the negative electric field gives rise to a shift in the CBM of the $MoTe_2/MoS_2$ heterostructure from the MoS_2 to the $MoTe_2$ layer. Meanwhile, the VBM of the $MoTe_2/MoS_2$ heterostructure remains at the Γ point and is contributed by the $MoTe_2$ layer. These findings predict that the $MoTe_2/MoS_2$ heterostructure changes to form a type I band alignment. In addition, when a positive electric field is applied, both the CBM and VBM of the $MoTe_2/MoS_2$ heterostructure move towards the Fermi level, leading to a reduction in the band gap. At a critical strength of the positive electric field of +0.38 V nm^{-1}, a transition from semiconductor to semimetal can be achieved in the $MoTe_2/MoS_2$ heterostructure, as its VBM crosses the Fermi level. Furthermore, it should be mentioned that a high strength electric field can be generated from the tabletop terahertz source within an electrolyte top gate.[58] Additionally, a high strength electric field always requires high-*k* and a back (top)-gated device architecture.[59] All these findings prove that the electric field can be considered as an effective tool to manipulate the electronic properties and contact type of the $MoTe_2/MoS_2$ heterostructure, thereby expanding its potential applications in electronics and optoelectronics.[60]

The biaxial in-plane strain is derived from $\varepsilon_b = (a - a_0)/a_0 \times 100\%$, where a and a_0 are the lattice parameters of the $MoTe_2/MoS_2$ heterostructure with and without the application of the biaxial strain, respectively. The negative and positive values refer to the compressive and tensile strains, respectively. The schematic model of the in-plane biaxial strain is depicted in the inset of Fig. 6. It is obvious that the strain causes a change in both the band gap values and contact types of the $MoTe_2/MoS_2$ heterostructure. The biaxial strain gives rise to a reduction in the band gap of the $MoTe_2/MoS_2$ heterostructure, as depicted in Fig. 6(a). The band gap of the $MoTe_2/MoS_2$ heterostructure can be reduced down to zero under the application of either a compressive strain of -12% or a tensile strain of +16%. This observation indicates that the transition from semiconductor to metal can be achieved in the $MoTe_2/MoS_2$ heterostructure under the application of biaxial strain. Additionally, the tensile strain can also lead to the transformation between type II and type I band alignment in the $MoTe_2/MoS_2$ heterostructure.

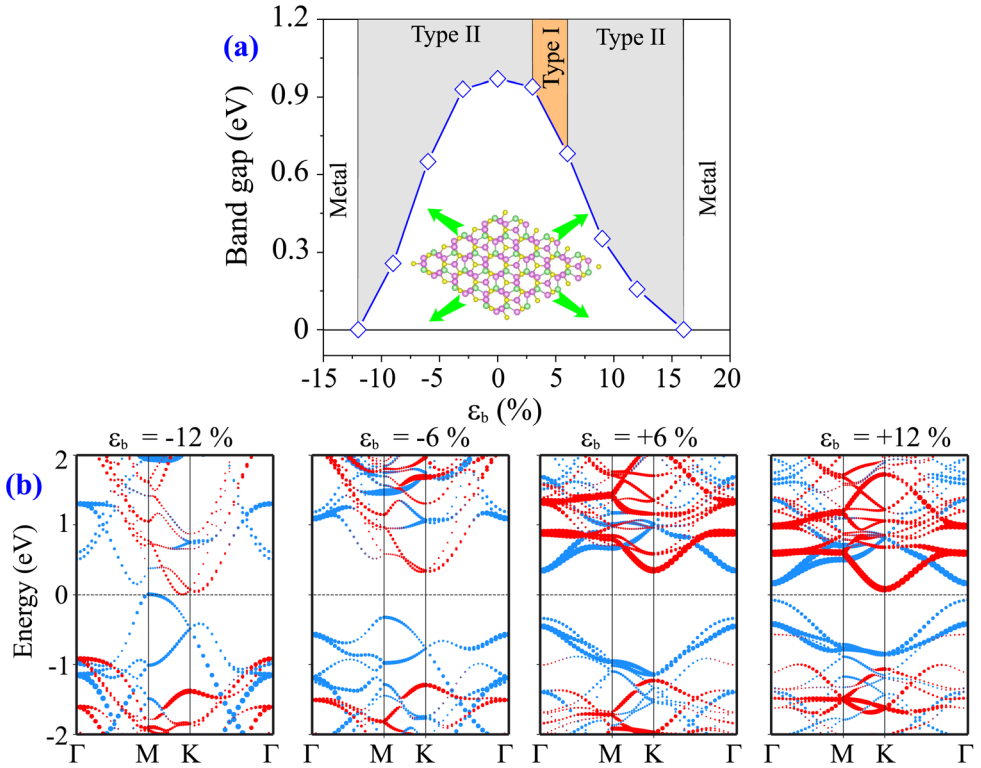

Fig. 6 (a) The variation of the band gaps and (b) the projected band structures of the $MoTe_2/MoS_2$ heterostructure under different ratios of strain. The inset shows the schematic model of the applied in-plane biaxial strain to the heterostructure.

To have a better understanding of the impact of the strain, we further analyze the projected band structures of the $MoTe_2/MoS_2$ heterostructure under different strain ratios, as illustrated in Fig. 6(b). When the compressive strain is applied, both the VBM and CBM of the $MoTe_2/MoS_2$ heterostructure shift towards the Fermi level, giving rise to a reduction in the band gap values. Similarly, the band edges of both the $MoTe_2$ and MoS_2 layers in the $MoTe_2/MoS_2$ heterostructure move closer to the Fermi level under the tensile strain. Under a tensile strain of $\varepsilon_b = +3\%$, the CBM of the $MoTe_2/MoS_2$ heterostructure shifts from the K to the Γ point. Thus, the indirect-to-direct transition is achieved in the $MoTe_2/MoS_2$ heterostructure. In addition, both the VBM and CBM of the $MoTe_2/MoS_2$ heterostructure now come from the $MoTe_2$ layer, indicating that there occurs a transition from type II to type I band alignment. The type I band alignment is maintained in the $MoTe_2/MoS_2$ heterostructure under tensile strains ranging from +3% to +6%. When the tensile strain is larger than +6%, the CBM of the $MoTe_2/MoS_2$ heterostructure is recovered from the Γ to the K point, while the VBM is preserved at the Γ point. This recovery indicates that there is a transition from direct to indirect semiconductor and a conversion from type I to type II band alignment because the band edges of the $MoTe_2/MoS_2$ heterostructure are contributed by the $MoTe_2$ layer. When the tensile strain is larger than 16%, the band edges of the $MoTe_2/MoS_2$ heterostructure cross the Fermi level, leading to a transition from semiconductor to metal. Our findings prove that the in-plane biaxial strain can effectively be used to tailor the electronic properties and contact types in the $MoTe_2/MoS_2$ heterostructure, thereby expanding its potential applications in multifunctional devices.

4 Conclusions

In conclusion, we have performed first-principles calculations to design a 2D vdW $MoTe_2/MoS_2$ heterostructure with the formation of a type II band alignment. Our results indicate that the $MoTe_2/MoS_2$ heterostructure is structurally, thermally and mechanically stable. The weak vdW interactions are found to be dominated at the interface of the $MoTe_2/MoS_2$ heterostructure and thus it can be synthesized in recent experiments by the transfer method or chemical vapor deposition. The vdW $MoTe_2/MoS_2$ heterostructure exhibits a staggered type II band alignment, effectively separating the electrons and holes at the interface and thereby extending the carrier lifetime. Furthermore, our findings reveal that the electronic properties and contact types of type II vdW $MoTe_2/MoS_2$ heterostructures can be tailored under the application of external conditions, including an electric field and in-plane biaxial strain. The semiconductor–semimetal–metal transition and type II–type I conversion can be achieved in the vdW $MoTe_2/MoS_2$ heterostructure. Our findings underscore the potential of the vdW $MoTe_2/MoS_2$ heterostructure for the design and fabrication of multifunctional applications, including electronics and optoelectronics.

Conflicts of interest

There are no conflicts to declare.

Acknowledgements

This research is funded by the Vietnam Ministry of Education and Training under Grant No. B2023.DNA.06.

References

1 K. S. Novoselov, A. K. Geim, S. V. Morozov, D.-e. Jiang, Y. Zhang, S. V. Dubonos, I. V. Grigorieva and A. A. Firsov, *Science*, 2004, **306**, 666–669.
2 A. S. Sarkar and E. Stratakis, *Adv. Sci.*, 2020, **7**, 2001655.
3 M. Yu, M. Hilse, Q. Zhang, Y. Liu, Z. Wang and S. Law, *ACS Appl. Nano Mater.*, 2024, DOI: **10.1021/acsanm.3c05984**.
4 S. Manzeli, D. Ovchinnikov, D. Pasquier, O. V. Yazyev and A. Kis, *Nat. Rev. Mater.*, 2017, **2**, 1–15.
5 R. Yang, Y. Fan, Y. Zhang, L. Mei, R. Zhu, J. Qin, J. Hu, Z. Chen, Y. Hau Ng, D. Voiry, *et al.*, *Angew. Chem., Int. Ed.*, 2023, **62**, e202218016.
6 Y. Wang, T. Guo, Z. Tian, K. Bibi, Y.-Z. Zhang and H. N. Alshareef, *Adv. Mater.*, 2022, **34**, 2108560.
7 Y. Gogotsi and B. Anasori, *The Rise of MXenes*, 2019.
8 Y. Gogotsi, *The Future of MXenes*, 2023.
9 Y. Wang, L. Liu, T. Ma, Y. Zhang and H. Huang, *Adv. Funct. Mater.*, 2021, **31**, 2102540.
10 N. Rono, J. K. Kibet, B. S. Martincigh and V. O. Nyamori, *Crit. Rev. Solid State Mater. Sci.*, 2021, **46**, 189–217.
11 L. Jiang, X. Yuan, Y. Pan, J. Liang, G. Zeng, Z. Wu and H. Wang, *Appl. Catal., B*, 2017, **217**, 388–406.
12 J. Kim, Y. Lee, M. Kang, L. Hu, S. Zhao and J.-H. Ahn, *Adv. Mater.*, 2021, **33**, 2005858.
13 X. Liu and M. C. Hersam, *Nat. Rev. Mater.*, 2019, **4**, 669–684.
14 N. P. De Leon, K. M. Itoh, D. Kim, K. K. Mehta, T. E. Northup, H. Paik, B. Palmer, N. Samarth, S. Sangtawesin and D. W. Steuerman, *Science*, 2021, **372**, eabb2823.
15 W. Huh, D. Lee and C.-H. Lee, *Adv. Mater.*, 2020, **32**, 2002092.
16 A. K. Geim and I. V. Grigorieva, *Nature*, 2013, **499**, 419–425.
17 Y. Liu, N. O. Weiss, X. Duan, H.-C. Cheng, Y. Huang and X. Duan, *Nat. Rev. Mater.*, 2016, **1**, 1–17.
18 K. Novoselov, A. Mishchenko, A. Carvalho and A. Castro Neto, *Science*, 2016, **353**, aac9439.
19 S.-J. Liang, B. Cheng, X. Cui and F. Miao, *Adv. Mater.*, 2020, **32**, 1903800.
20 R. Cheng, F. Wang, L. Yin, Z. Wang, Y. Wen, T. A. Shifa and J. He, *Nat. Electron.*, 2018, **1**, 356–361.
21 J. Kim, D. Rhee, O. Song, M. Kim, Y. H. Kwon, D. U. Lim, I. S. Kim, V. Mazánek, L. Valdman, Z. Sofer, *et al.*, *Adv. Mater.*, 2022, **34**, 2106110.
22 J. Li, X. Yang, Y. Liu, B. Huang, R. Wu, Z. Zhang, B. Zhao, H. Ma, W. Dang, Z. Wei, *et al.*, *Nature*, 2020, **579**, 368–374.
23 V. Selamneni and P. Sahatiya, *Microelectron. Eng.*, 2023, **269**, 111926.
24 K. Nasrin, V. Sudharshan, K. Subramani and M. Sathish, *Adv. Funct. Mater.*, 2022, **32**, 2110267.
25 F. Liu, S. Jin, Q. Xia, A. Zhou and L.-Z. Fan, *J. Energy Chem.*, 2021, **62**, 220–242.
26 Y. Yin, Q. Gong, M. Yi and W. Guo, *Adv. Funct. Mater.*, 2023, **33**, 2214050.
27 C. C. Tho, S.-D. Guo, S.-J. Liang, W. L. Ong, C. S. Lau, L. Cao, G. Wang and Y. S. Ang, *Appl. Phys. Rev.*, 2023, **10**, 041307.
28 J. E. Padilha, A. Fazzio and A. J. da Silva, *Phys. Rev. Lett.*, 2015, **114**, 066803.
29 M. Batmunkh, M. Bat-Erdene and J. G. Shapter, *Adv. Mater.*, 2016, **28**, 8586–8617.
30 K. Ren, M. Sun, Y. Luo, S. Wang, J. Yu and W. Tang, *Appl. Surf. Sci.*, 2019, **476**, 70–75.
31 M.-H. Chiu, C. Zhang, H.-W. Shiu, C.-P. Chuu, C.-H. Chen, C.-Y. S. Chang, C.-H. Chen, M.-Y. Chou, C.-K. Shih and L.-J. Li, *Nat. Commun.*, 2015, **6**, 7666.
32 J. H. Yu, H. R. Lee, S. S. Hong, D. Kong, H.-W. Lee, H. Wang, F. Xiong, S. Wang and Y. Cui, *Nano Lett.*, 2015, **15**, 1031–1035.
33 M. Son, H. Jang, D.-B. Seo, J. H. Lee, J. Kim, M. Kim, S. Kang, S. Yim, W. Song, J.-W. Yoo, *et al.*, *Adv. Funct. Mater.*, 2024, **34**, 2308906.
34 Y. Xue, Y. Zhang, Y. Liu, H. Liu, J. Song, J. Sophia, J. Liu, Z. Xu, Q. Xu, Z. Wang, *et al.*, *ACS Nano*, 2016, **10**, 573–580.
35 J. Ahn, J.-H. Kyhm, H. K. Kang, N. Kwon, H.-K. Kim, S. Park and D. K. Hwang, *ACS Photonics*, 2021, **8**, 2650–2658.
36 M. Huang, S. Li, Z. Zhang, X. Xiong, X. Li and Y. Wu, *Nat. Nanotechnol.*, 2017, **12**, 1148–1154.
37 Y. Huang, Y.-H. Pan, R. Yang, L.-H. Bao, L. Meng, H.-L. Luo, Y.-Q. Cai, G.-D. Liu, W.-J. Zhao, Z. Zhou, *et al.*, *Nat. Commun.*, 2020, **11**, 2453.
38 H. G. Kim and H.-B.-R. Lee, *Chem. Mater.*, 2017, **29**, 3809–3826.
39 Z. Cai, B. Liu, X. Zou and H.-M. Cheng, *Chem. Rev.*, 2018, **118**, 6091–6133.
40 Y. Ding, N. Zhou, L. Gan, X. Yan, R. Wu, I. H. Abidi, A. Waleed, J. Pan, X. Ou, Q. Zhang, *et al.*, *Nano Energy*, 2018, **49**, 200–208.
41 X. Ji, Z. Bai, F. Luo, M. Zhu, C. Guo, Z. Zhu and S. Qin, *ACS Omega*, 2022, **7**, 10049–10055.
42 Y. Chen, X. Wang, G. Wu, Z. Wang, H. Fang, T. Lin, S. Sun, H. Shen, W. Hu, J. Wang, *et al.*, *Small*, 2018, **14**, 1703293.
43 A. Pezeshki, S. H. H. Shokouh, T. Nazari, K. Oh and S. Im, *Adv. Mater.*, 2016, **28**, 3216–3222.
44 P. Giannozzi, S. Baroni, N. Bonini, M. Calandra, R. Car, C. Cavazzoni, D. Ceresoli, G. L. Chiarotti, M. Cococcioni, I. Dabo, *et al.*, *J. Phys.: Condens.Matter*, 2009, **21**, 395502.
45 P. Giannozzi, O. Andreussi, T. Brumme, O. Bunau, M. B. Nardelli, M. Calandra, R. Car, C. Cavazzoni, D. Ceresoli, M. Cococcioni, *et al.*, *J. Phys.: Condens.Matter*, 2017, **29**, 465901.
46 J. P. Perdew, K. Burke and M. Ernzerhof, *Phys. Rev. Lett.*, 1998, **80**, 891.
47 G. Kresse and D. Joubert, *Phys. Rev. B: Condens. Matter Mater. Phys.*, 1999, **59**, 1758.
48 J. Heyd, G. E. Scuseria and M. Ernzerhof, *J. Chem. Phys.*, 2003, **118**, 8207–8215.
49 S. Grimme, J. Antony, S. Ehrlich and H. Krieg, *J. Chem. Phys.*, 2010, **132**, 154104.
50 J. A. Wilson and A. Yoffe, *Adv. Phys.*, 1969, **18**, 193–335.
51 K. Tang, W. Qi, Y. Li and T. Wang, *J. Phys. Chem. C*, 2018, **122**, 7027–7032.

52 H. Shu, M. Zhao and M. Sun, *ACS Appl. Nano Mater.*, 2019, **2**, 6482–6491.
53 Y. Luo, K. Ren, S. Wang, J.-P. Chou, J. Yu, Z. Sun and M. Sun, *J. Phys. Chem. C*, 2019, **123**, 22742–22751.
54 Z. Liu, J. Z. Liu, Y. Cheng, Z. Li, L. Wang and Q. Zheng, *Phys. Rev. B*, 2012, **85**, 205418.
55 L. A. Girifalco and M. Hodak, *Phys. Rev. B: Condens. Matter Mater. Phys.*, 2002, **65**, 125404.
56 J. Wang, L. Bai, X. Zhao, C. Chen and L. Niu, *Phys. E*, 2023, **149**, 115668.
57 F. Mouhat and F.-X. Coudert, *Phys. Rev. B: Condens. Matter Mater. Phys.*, 2014, **90**, 224104.
58 C. Vicario, B. Monoszlai and C. P. Hauri, *Phys. Rev. Lett.*, 2014, **112**, 213901.
59 J. Robertson, *Eur. Phys. J.: Appl. Phys.*, 2004, **28**, 265–291.
60 C. W. Tan, L. Xu, C. C. Er, S.-P. Chai, B. Kozinsky, H. Y. Yang, S. A. Yang, J. Lu and Y. S. Ang, *Adv. Funct. Mater.*, 2024, **34**, 2308679.